HHS Public Access

Author manuscript

Free Radic Biol Med. Author manuscript; available in PMC 2024 January 01.

Published in final edited form as:

Free Radic Biol Med. 2023 January ; 194: 23–32. doi:10.1016/j.freeradbiomed.2022.11.025.

Skeletal muscle Nox4 knockout prevents and Nox2 knockout blunts loss of maximal diaphragm force in mice with heart failure with reduced ejection fraction

Ravi A. Kumar[a,b], **Dongwoo Hahn**[a,c], **Rachel C. Kelley**[a,d], **Derek R. Muscato**[a], **Alex Shamoun**[a], **Nuria Curbelo-Bermudez**[a], **W. Greyson Butler**[a], **Svetlana Yegorova**[a], **Terence E. Ryan**[a], **Leonardo F. Ferreira**[a,*]

[a] Department of Applied Physiology and Kinesiology, University of Florida, Gainesville, FL, USA

[b] King's College London British Heart Foundation Centre of Excellence, School of Cardiovascular Medicine & Sciences, London, United Kingdom

[c] Department of Integrative Biology and Physiology, University of Minnesota, Minneapolis, MN, USA

[d] Endocrine Society, Washington, D.C, USA

Abstract

Patients with heart failure with reduced ejection fraction (HFrEF) experience diaphragm weakness that contributes to the primary disease symptoms of fatigue, dyspnea, and exercise intolerance. Weakness in the diaphragm is related to excessive production of reactive oxygen species (ROS), but the exact source of ROS remains unknown. NAD(P)H Oxidases (Nox), particularly the Nox2 and 4 isoforms, are important sources of ROS within skeletal muscle that contribute to optimal cell function. There are reports of increased Nox activity in the diaphragm of patients and animal models of HFrEF, implicating these complexes as possible sources of diaphragm dysfunction in HFrEF. To investigate the role of these proteins on diaphragm weakness in HFrEF, we generated inducible skeletal muscle specific knockouts of Nox2 or Nox4 using the Cre-Lox system and assessed diaphragm function in a mouse model of HFrEF induced by myocardial infarction. Diaphragm maximal specific force measured in vitro was depressed by ~20% with HFrEF. Skeletal muscle knockout of Nox4 provided full protection against the loss of maximal force ($p < 0.01$), while the knockout of Nox2 provided partial protection (7% depression, $p < 0.01$). Knockout of Nox2 from skeletal myofibers improved survival from 50 to 80% following myocardial infarction ($p = 0.026$). Our findings show an important role for skeletal muscle NAD(P)H Oxidases contributing to loss of diaphragm maximal force in HFrEF, along with systemic pathophysiological responses following myocardial infarction.

* Corresponding author. Department of Applied Physiology and Kinesiology University of Florida, 1864 Stadium Rd, room 100 FLG, Gainesville, FL, 32611-8205, USA. ferreira@ufl.edu (L.F. Ferreira).

Declaration of competing interest

The authors have no conflict of interest.

Appendix A. Supplementary data

Supplementary data to this article can be found online at https://doi.org/10.1016/j.freeradbiomed.2022.11.025.

Keywords

NADPH Oxidases; Diaphragm; Heart failure; HFrEF; Muscle; Weakness

1. Introduction

Heart failure with reduced ejection fraction (HFrEF) causes inspiratory dysfunction that contributes to the pathophysiology of the disease [1]. Patients with HFrEF display reduced inspiratory muscle strength and endurance that worsens with disease severity [1–4]. Maximal inspiratory pressure (MIP), a metric of inspiratory muscle strength, is an important indicator of clinical outcomes in patients with HFrEF: MIP is a better predictor of all-cause mortality than 6-min walking distance and left ventricular ejection fraction [5], and patients that improved MIP following a cardiac rehabilitation program that included inspiratory muscle training had a lower risk of hospital re-admission or death than subjects that showed no improvement [6]. These studies highlight the importance of inspiratory muscle function and indicate that not all patients with HFrEF will respond to and benefit from inspiratory muscle training to improve inspiratory function [6]. Thus, further understanding of the mechanisms leading to inspiratory muscle dysfunction is critical for developing targeted treatments to improve mortality and quality of life in patients with HFrEF.

The diaphragm is the primary inspiratory muscle, and dysfunction in this skeletal muscle contributes to the inspiratory dysfunction seen in HFrEF. Diaphragm biopsies from patients and extensive work in animal models suggest contractile dysfunction underpins diaphragm abnormalities in HFrEF, along with reports of muscle atrophy, fiber-type shifts, and altered mitochondrial function [7–14].

Reactive oxygen species (ROS) are key mediators of diaphragm dysfunction in HFrEF: increased markers of protein oxidation and intracellular redox shifts have been observed in the diaphragm of patients and animal models of HFrEF [7,8,13,15,16] but the source of excess ROS remains unknown. NAD(P)H oxidases (Nox), specifically the Nox2 and 4 isoforms, are important sources of ROS in skeletal muscle [17–19]. Nox2 is activated by phosphorylation of its assembly subunit, $p47^{phox}$, which coordinates the localization of several subunits to the sarcolemma and t-tubules [19]. Diaphragm biopsies from patients and animal models of HFrEF show increased abundance of Nox2 subunits and phosphorylation of $p47^{phox}$ [9,13,15], implicating Nox2 as a primary source of ROS leading to diaphragm dysfunction. Whole-body knockout of $p47^{phox}$ prevented the development of diaphragm contractile dysfunction in HFrEF [9] but this protection could have originated from other cell types with high Nox2 activity such as immune cells [20]. Nox4, localized primarily in the mitochondria and sarcoplasmic reticulum [19], is constitutively active and produces intracellular H_2O_2 dependent on its protein abundance [21]. Nox4 protein abundance is increased in the diaphragm of patients with heart failure [13]. A recent report established a signaling axis in muscular dystrophy that involves crosstalk between Nox4 and Nox2 contributing to skeletal muscle weakness where the levels of Nox4 can impact the levels of Nox2 [22]. Increased Nox2 and Nox4 activity may also further ROS emission from

mitochondria [23], which is evident in the diaphragm from rat models of HFrEF [8,12,16], and cause post-translational modifications that impair mitochondrial respiration.

The aim of the current study was to test the hypothesis that skeletal myocyte-specific Nox2 and Nox4 contribute to diaphragm contractile dysfunction and examine the Nox2-Nox4 interactions and mitochondrial crosstalk in HFrEF. Following skeletal muscle-specific knockout of Nox2 or Nox4, we measured diaphragm contractile properties, fiber size, and mitochondrial function (respiration and ROS) in a mouse model of HFrEF resulting from ischemic cardiomyopathy induced by myocardial infarction. Our main findings reveal a contribution of both Nox2 and Nox4 to loss of maximal force, are consistent with Nox4-dependent regulation of Nox2 mRNA, and do not support a Nox-mitochondria crosstalk in the diaphragm of heathy or HFrEF mice.

2. Methods

2.1. Animals

All procedures performed in animals followed guidelines established by the National Institutes of Health and were approved by the Institutional Animal Care and Use Committee of the University of Florida (Protocol #201809075). Animals were housed at our institution's facilities under a 12-h:12-h light-dark cycle with access to standard chow and water *ad libitum.*

Inducible skeletal muscle-specific Nox2 knockout (skmNox2^{KO}) male mice (n = 76) were generated by crossing mice carrying floxed Nox2 alleles (donated by Professor Ajay Shah [24]) with mice expressing an inducible Cre recombinase under the human skeletal actin (HSA) promoter (HSA-Cre) [25]. The Cre recombinase is flanked by a mutated estrogen receptor (Mer) ligand-binding domain (MerCreMer) that permits inducible activation via tamoxifen injection. Inducible skeletal muscle-specific Nox4 knockout (skmNox4^{KO}) male mice (n = 90) were generated by crossing mice carrying floxed Nox4 alleles (donated by Professor Junichi Sadoshima [26]) with mice expressing HSA-Cre. Once activated, the Cre recombinase identifies the loxP recognition sites flanking the Nox2 or Nox4 gene and excises that sequence in skeletal muscle. At approximately 8–10 weeks of age, mice received tamoxifen (5 consecutive days, 40 mg/kg body weight dissolved in ethanol, delivered in 100 μl sunflower oil) (skmNox2^{KO}; skmNox4^{KO}) or vehicle solution (100 μl sunflower oil) (skmNox2$^{+/y}$; skmNox4$^{+/+}$) through intraperitoneal injections [27]. Mice were randomly assigned to KO or control groups. The mouse diaphragm has a higher satellite cell content than limb muscle and sees a continuous contribution of satellite cells to the myonuclear pool over time, even under sedentary, non-stressed conditions [28,29]. To maintain knockout of Nox2 or Nox4 in the presence of ongoing satellite cell fusion across the experimental time frame, we additionally administered recombinant adeno-associated virus serotype 9 (rAAV9) containing HSA-Cre (to skmNox2^{KO} and skmNox4^{KO}) or an empty vector (to skmNox2$^{+/y}$ and skmNox4$^{+/+}$) through a single intra-cardiac injection (~1 × 10^{11} vector genomes in 200 μl sterile saline) in the ventricular chamber two weeks following tamoxifen or vehicle injections. We anesthetized mice with an oxygen-isoflurane mixture (5% induction, 2–3% maintenance), removed hair from the abdomen and thorax, cleaned the area with chlorhexidine and sterile saline, and placed the mice in a supine

position. A 31-gauge needle containing the virus-saline mixture was inserted beneath the xyphoid process while applying gentle suction, angled cranially and slightly to the left of the sternum. Upon seeing blood return in the syringe, we slowly injected the virus.

Skeletal muscle-specific deletion of Nox2 was confirmed by polymerase chain reaction using primers from Sag et al. (2017). We extracted DNA from diaphragm, gastrocnemius, left ventricle, and liver tissue samples. Skeletal muscle Nox2 deletion was confirmed by amplification of a 225 base pair product that is present following recombination. Non-skeletal muscle tissues and skmNox2$^{+/y}$ animals that did not receive tamoxifen displayed a 567 base pair product.

Skeletal muscle-specific deletion of Nox4 was confirmed by polymerase chain reaction based on the amplification of a ~1600 base pair product that forms after the excision of exon 9 of the Nox4 gene (forward primer, aacactgttggactcttcagacaca; reverse primer, ctcctgatgcatcggtaaagtc). Non-skeletal muscle tissues and skmNox4$^{+/+}$ animals that did not receive tamoxifen do not display an amplified product, indicating that no recombination or gene excision had occurred.

Male mice were used in these experiments because of the higher incidence of HFrEF resulting from myocardial infarction in men [30]. There is currently no scientific reason to expect differences between men and women regarding the development of diaphragm weakness as women diagnosed with HFrEF also experience inspiratory insufficiency, and female mice develop diaphragm weakness post-myocardial infarction [31].

2.2. Surgery

Heart failure with reduced ejection fraction (HFrEF) was induced by myocardial infarction (MI) as previously described [9,12]. Four weeks after tamoxifen or vehicle injection and two weeks after viral administration, animals were anesthetized with a 5% isoflurane-oxygen mixture and placed on mechanical ventilation with 2–3% maintenance isoflurane. We then performed a left thoracotomy to expose the heart and ligated the left anterior descending coronary artery with 6–0 monofilament absorbable PGA suture (DemeSORB; Demtec). The ribs were approximated with 6–0 PGA suture, and the skin incision closed with 3–0 suture (DemeLON; Demetech). Sham surgeries were identical to the MI procedure but without ligation of the coronary artery. Mice were randomly assigned to sham or MI procedures within genetic strains.

Animals immediately received subcutaneous buprenorphine and topical bupivacaine. Buprenorphine injections were maintained every 8–12 h for three days post-surgery. To minimize stress and enhance survival, animal cages were placed on a heating pad (set to maintain cage temperature at 32 °C) and received supplemental medical-grade oxygen (0.35 F_iO_2) via a large animal O_2 tent (Buster ICU; Kruuse; Langeskov, Denmark) for three days post-procedure.

2.3. Echocardiography

Two to four weeks before terminal experiments, we assessed cardiac function by echocardiography as described previously [9]. Mice were maintained under ~2% isoflurane

anesthesia (adjusted to keep heart rate between 400 and 500 bpm) while two-dimensional M-mode ultrasound images were obtained in the parasternal short axis view (Aplio; Toshiba America Medical Systems, Tusin, CA). We determined left ventricular internal diameter during diastole (LVIDd) and systole (LVIDs) using Image J software. Fractional shortening (%) was calculated as (LVIDd – LVIDs)/LVIDd × 100. All echocardiography measures were completed between 17:00 and 21:00 h.

2.4. Tissue harvesting and infarct size

Terminal experiments were conducted 14–16 weeks post-surgery and commenced between 08:30 h and 09:30 h. We anesthetized mice using isoflurane (5% induction, 2–3% maintenance) and performed a laparotomy and thoracotomy to collect tissue samples while the animals were in the surgical place of anesthesia.

We excised the diaphragm and heart and placed them in ice-cold bicarbonate-buffered solution (in mM: 137 NaCl, 5 KCl, 1 MgSO4, 1 NaH2PO4, 24 NaHCO3, and 2 CaCl2). Portions of the costal diaphragm were allocated for contractile, mitochondrial, and histological analyses. The remaining diaphragm was flash frozen in liquid nitrogen and stored at −80 °C for later biochemical assays.

Ventricles were separated, weighed, and the left ventricle was cut down the interventricular septum from the base to the apex to determine infarct size by planimetry [9,32]. Inspiratory dysfunction worsens with the severity of HFrEF in patients [1] and diaphragm dysfunction is prevalent in rodents with severe HFrEF [7]. For this reason, we restricted our HFrEF experimental groups to mice displaying severe HFrEF, defined as infarcted left ventricle area greater than 30% [33] and right ventricle weight/body weight ratio two standard deviations greater than sham group average (indicative of right ventricular hypertrophy secondary to pulmonary arterial hypertension) [7,34].

2.5. Diaphragm contractile properties in vitro

We assessed diaphragm contractile properties in an isolated diaphragm strip as previously described [35]. A diaphragm strip was fixed between a glass rod and a dual-mode lever system (300C-LR; Aurora Scientific, Aurora, ON, Canada) and placed in a water-jacketed organ bath containing bicarbonate-buffered solution that was continuously gassed with 95% O_2/5% CO_2 at room temperature. Muscle contractile properties were assessed with a high-power biphasic stimulator (701c; Aurora Scientific) sending a supramaximal current (600 mA current; 0.25 ms pulse width; 0.3 s train duration) through two platinum electrodes flanking the muscle. We adjusted the length of the muscle to elicit maximal tetanic force (120 Hz) (optimal length; L_o) and increased the temperature of the bath to 37 °C. Following a 10-min thermal equilibrium period, we measured diaphragm force at L_o during isometric contractions at frequencies of 1, 30, 50 and 300 Hz, separated by 1 min rest intervals. The mouse diaphragm is approximately 250–500 μm thick, which is within the limitations of oxygen and substrate diffusion at 37 °C when bathing solution is gassed with 95% O_2 [36]. These conditions avoid the development of an anoxic core and preserve the stability of the preparation for longer experiments.

We measured muscle length at L_o using electronic calipers and determined muscle bundle weight. Force was normalized to muscle cross sectional area, calculated by muscle weight divided by the product of length and density of mammalian skeletal muscle [37].

2.6. Isolation and permeabilization of diaphragm fiber bundles for mitochondrial assessment

Diaphragm muscle bundles were prepared to assess mitochondrial function as recently described [38]. A portion of the right hemi-diaphragm was dissected with fine tweezers in ice-cold Buffer X (in mM: 7.23 K_2EGTA, 2.77 Ca–K_2EGTA, 20 imidazole, 20 taurine. 5.7 ATP, 14.3 PCr, 6.56 $MgCl_2$–$6H_2O$, 50 K-MES; pH 7.1) to remove branches of the phrenic nerve, and the abdominal layer of fascia and muscle fibers. The remaining pleural layer of fibers was then teased apart longitudinally to expose optimal surface area of fibers without inducing damage. We then permeabilized the bundles in Buffer X containing saponin (30 μg/ml) for 30 min at 4 °C. Bundles were washed 3 × 5 min in buffer Z (in mM: 30 KCl, 10 KH_2PO_4, 5 $MgCl_2$–$6H_2O$, 105 K-MES, and 0.5 mg/ml BSA, pH 7.1), after which we proceeded with assessment of mitochondrial respiration or substrate-induced H_2O_2 emission.

2.7. Mitochondrial respiration

We performed high-resolution O_2 respirometry at 37 °C in buffer Z with 20 mM creatine monohydrate and 10 μM Blebbistatin using an O2K Oxygraph (Oroboros, Innsbruck, Austria). We used a substrate-inhibitor titration protocol to measure oxygen flux (JO_2) under the following incremental conditions: 0.5 mM malate + 10 mM glutamate, ADP (0.5 mM, 8 mM), 10 mM Cytochrome C, 10 mM succinate, and 10 μM rotenone. Oxygen concentration in the assay buffer was brought up to ~400 μM at the start of each experiment and re-oxygenated when O_2 content dropped below 250 μM. Bundles were immediately blotted dry, flash frozen in liquid nitrogen, and stored at −80 °C for later measurements of total protein and immunoblotting experiments. Oxygen flux (JO_2, pmol/s) was normalized by bundle total protein. Two bundles from the same animal were run simultaneously and the results were averaged for statistical analysis. Respiratory control ratio (RCR) was calculated as the ratio of state III (maximal ADP stimulated; 8 mM ADP) to state II respiration (malate + glutamate). Bundles were excluded from final analyses if there was a >10% increase in JO_2 following the addition of cytochrome C, indicating fiber bundle damage.

2.8. Mitochondrial H_2O_2 emission

Substrate induced H_2O_2 emission was assessed in permeabilized diaphragm fiber bundles using a fluorometer ($\lambda_{excitation}$ = 565 nm, $\lambda_{emission}$ = 600 nm, Fluorolog-3; Horiba Jobin Yvon, Edison, NJ) as previously described [12,38]. Bundles were placed into a quartz cuvette containing Buffer Z with 10 μM Amplex Ultra Red (Life Technologies, Eugene, OR), 25 μM Blebbistatin, 1 mM EGTA, 30 U/ml superoxide dismutase, and 1 U/ml horseradish peroxidase that was heated to 37 °C and continuously stirred with a magnetic stir bar. We measured Amplex Ultra Red fluorescence under baseline conditions followed by the addition of 10 mM succinate. Amplex Ultra Red fluorescence was converted to H_2O_2 emission (JH_2O_2) using a standard curve that was determined after each experiment.

Bundles were immediately blotted dry and weighed for data normalization (JH_2O_2: pmol/s/mg WW).

2.9. rtPCR

We isolated RNA from tissue samples using the Direct-Zol RNA Microprep kit from Zymo Research (Irvine, CA). Samples were homogenized in TRI-Reagent (T9424; Sigma Aldrich) using stainless steel beads and a bullet blender (BBY24 M; Next Advanced, Troy, NY). We assessed RNA quantity and quality via UV spectroscopy (Nanodrop 2000; ThermoFisher), then generated cDNA using the Superscript IV First-Strand synthesis system (18091050; Invitrogen). Real time PCR was performed on a Quantstudio 3 thermocycler (Thermo Fisher) using Taqman Universal Master Mix II (4440040; ThermoFisher) and Taqman probes (all from Thermo Fisher) for Nox4 (Mm00479246_m1), Nox2 (*CYBB;* Mm01287743_m1) and $p47^{phox}$ (*NCF1;* Mm00447921_m1). Results using Taqman probes were normalized to *HPRT* (Mm00446968_m1). Because the Taqman probes used in these experiments target exons that are still transcribed following genetic recombination, we completed additional experiments using SYBR Green (4309155; ThermoFisher) and primers specifically targeted to areas of recombination in the Nox2 and Nox4 models. For detecting Nox2 in the Nox2 floxed model, we used primers targeted to exons 1 and 2 (F: AGA GAG GCA GAA CCA ACA CT; R: CCC CAA CCA CAC CAG AAT GA). For detecting Nox4 in the Nox4 floxed model, we used primers targeted to exons 8 and 9 (F: GCT CAT TTC CCA CAG ACC TGG; R: GGT GAC AGG TTT GTT GCT CCT). These results were normalized to HPRT expression (F: CTC ATG GAC TGA TTA TGG ACA GGA C; R: GCA GGT CAG CAA AGA ACT TAT AGC C). Gene expression was calculated relative to the skmNox4-sham or skmNox2-sham group using the $\Delta\Delta C_T$ method.

2.10. Gel electrophoresis and immunoblotting

To assess protein abundance via immunoblotting, diaphragm samples were homogenized 1:10 w:v in RIPA Buffer (50 mM Tris [pH 7.5], 150 mM NaCl, 0.075% NaDoC, 1% IGEPAL CA-60) with 1x Halt protease and phosphatase inhibitors (78440; ThermoFisher) on ice using Dual Kontes glass tissue grinders. We centrifuged the homogenates (16,000×*g*, 15 min, 4 °C), then determined the protein content of the resulting supernatant using the DC Assay (Bio-Rad). Supernatants were then diluted 3:1 with 4x Laemmli sample buffer (125 mM Tris-HCl [pH 6.8], 20% glycerol, 4% SDS, 10% 2-mercaptoethanol, and 0.02% bromophenol blue).

We prepared additional tissue homogenates using diaphragm fiber bundles from mitochondrial respiration experiments to assess differences in mitochondrial electron transport system complexes and citrate synthase content. We homogenized fiber bundles in 40 μl of 1x Laemmli Buffer (Bio-Rad) containing 0.35 M DTT at room temperature using a Dual Kontes plastic tissue homogenizer attached to an electric drill (30 s, high torque setting). Homogenates were centrifuged at 1,000×*g* for 10 min at room temperature and the resulting supernatant was transferred to a fresh tube. We determined protein content of the lysate via gel electrophoresis (described below) using a 3-point bovine serum albumin (BSA) standard curve. Total protein content of each individual bundle was determined by multiplying the calculated protein content (μg/μl) by 40 μl, the initial dilution volume.

For gel electrophoresis, we ran similar amounts of protein per lane (~10–20 μg, depending on target) on a 4–20% Criterion TGX stain-free gel (Bio-Rad) at 200 V for 50 min with the cassette surrounded by ice. Gels were activated and scanned using a Gel Doc EZ imager (Bio-rad) for determination of total protein per lane, after which proteins were transferred onto a nitrocellulose membrane at a current of 200 mA for 2 h at 4 °C. Following transfer, the membrane was washed for 5 min in TBS, then blocked in Intercept blocking buffer (LI-COR, Lincoln, NE) for 1 h at room temperature. We then incubated membranes in primary antibodies diluted in blocking buffer with 1% TWEEN-20 overnight at 4 °C. Primary antibodies included citrate synthase (1:1,000 dilution ab96600; Abcam, Cambridge, MA), OXPHOS antibody cocktail (1:1,000 dilution ab110413; Abcam), and RyR1 (1:500 dilution MA3–925; Invitrogen). Membranes were washed 4 × 5 min in TBS-T, then incubated with appropriately conjugated secondary antibodies ($IRDye_{800}$ 1:20,000 dilution; $IRDye_{680}$ 1:40,000 dilution – LI-COR) for 1 h at room temperature. After 4 × 5 min additional washes in TBS-T and 1 × 5 min rinse in TBS, membranes were scanned using an Odyssey Infrared Imaging System (LI-COR).

We used Image Lab 5.0 software (Bio-Rad) to quantify the total protein signal in each gel lane after gel electrophoresis. We quantified the immunoblot signal of target proteins using Image Studio Lite (LI-COR, Lincoln, NE). The immunoblot signal of each target protein was then normalized by the total protein signal measured in the corresponding lanes.

We tested the linear range for all antibodies used in this study using pooled samples and loaded protein contents that were approximately in the mid-portion of the linear range of detection for each antibody. Each gel and membrane included an abbreviated 3-point linearity to further confirm that individual samples were loaded within the linear range of detection.

2.11. Fiber type distribution and cross-sectional area

A diaphragm bundle was embedded in Tissue-Tek OCT freezing medium, frozen in liquid-nitrogen cooled-isopentane, and stored at −80 °C. Later, we prepared 10 μm cross-sections of diaphragm bundles using a cryostat (Leica, CM 2050S model) cooled to approximately −20 °C, transferred sections to frosted microscope slides, and followed a previously described protocol to stain for myosin heavy chain isoforms [7]. Briefly, we incubated slides in 1:2000 wheat germ agglutinin (WGA) Texas Red (Molecular Probes) and primary antibodies specific for myosin heavy chain Type I (A4.840, 1:15; Developmental Studies Hybridoma Bank) and Type IIa (SC-71, 1:50; Developmental Studies Hybridoma Bank). Sections were then incubated with fluorescently conjugated secondary antibodies (Goat × Mouse IgM Alexa 350 and Goat × Mouse IgG Alexa 488×, Invitrogen) and imaged using an inverted fluorescence microscope (Axio Observer, 10× objective lens) connected to a monochrome camera (Axio MRm) and controlled with Zen Pro software (Carl Zeiss Microscopy). We used the high throughput semi-automatic Myovision software [39] to quantify fiber cross sectional area and detect fiber types based on antibody detection. Fibers that were not detected by Type I or IIa antibodies were labeled as Type IIx.

2.12. Glutathione (GSH) content and redox state

We determined glutathione content and redox state using high-performance liquid chromatography as described previously [40,41]. Diaphragm samples were homogenized in perchloric acid with 0.2 M boric acid and 10 μM γ-glutamylglutamate using Dual Kontes tissue grinders, then sonicated and stored at −20 °C overnight. We then centrifuged the homogenates (16,000 g, 20 min, 4 °C) and stored the supernatant at −80 °C. After determining the protein content of the resulting pellet using the DC Assay (BioRad), we sent frozen supernatants for determination of GSH, CysGSH, and GSSG at the Emory Clinical Biomarkers Laboratory (Emory University, Atlanta, GA). Results were normalized by total protein content of the pellet. Oxidized glutathione content was determined by the sum of CysGSH content and 2 × GSSG content.

2.13. Statistics

Data in text and tables are presented as mean ± SD. Individual data (scatterplots) and group means (bars) are shown in figures unless stated otherwise. We performed tests for normality (Shapiro-Wilk) and equal variance (Brown-Forsythe), and log-transformed non-parametric data before running parametric statistical tests. We analyzed effects and interactions of surgical treatment (*factor 1*: sham vs. HFrEF) and genetic strain (*factor 2*: skmNox2/4$^{+/+}$ vs. skmNox2/4^{KO}) by two-way ANOVA. When there was a statistically significant interaction, we followed up with Bonferroni's test for post hoc comparisons (SigmaPlot v. 14.0; Systat Software, San Jose, CA). In select cases, we performed post-hoc analyses when the interaction effect did not reach significance based on previous recommendations [42]. We used unpaired Student's *t*-test (parametric) to compare infarct size between strains. For assessing differences in fiber cross-sectional area, we applied a linear mixed model analysis (SPSS v26 IBM, Armonk, NY) because of the variable number of fibers measured for each animal. Survival rates post-MI were compared using the Gehan-Breslow-Wilcoxon test. This test places greater weight on differences in survival at earlier time points if hazards ratios are not consistent over time, as is the case with mortality post-MI [34]. All statistical tests were conducted using two-tailed tests and statistical significance declared when $p < 0.05$. Wherever feasible, we report exact *p* values and have taken recent recommendations into consideration for our data interpretation [42–44].

3. Results

3.1. Experimental animals and induction of HFrEF

All animals included in final analyses displayed the anticipated PCR amplified products, indicating appropriate genetic strain and presence (KO) or absence (+/+ for Nox4, +/y for Nox2) of recombination by Cre recombinase (Fig. 1 A, B). mRNA abundance of *Nox4* increased with HFrEF but showed no change with Nox4^{KO} compared to vehicle injected shams (Fig. S1 A), whereas *Nox2* and *p47^{phox}* mRNA abundance decreased with skeletal muscle knockout of Nox4, regardless of surgical treatment (Fig. S1 B, C). In skmNox2$^{+/y}$ groups, Nox2 mRNA abundance decreased by 50% following genetic recombination, while HFrEF caused a decrease in *Nox4* and *Nox2* mRNA abundance (Fig. S1).

Characteristics of experimental animals are listed in Tables 1 and 2. For investigations into the effect of Nox4 on diaphragm function in HFrEF, a total of 76 animals underwent the MI procedure. Post-operative survival rate for skmNox4$^{+/+}$ and skmNox4^{KO} were not different (Fig. 2A). Based on infarct size and right ventricle/body weight ratio inclusion criteria for severe HFrEF, we assessed diaphragm function in seven skmNox4$^{+/+}$ (five excluded) and six skmNox4^{KO} (five excluded) HFrEF animals. The skmNox4$^{+/+}$ and skmNox4^{KO} sham surgery groups each contained seven animals. Thus, the total number of animals used for diaphragm analysis was n = 27.

For investigations into the effect of skmNox2 on diaphragm function in HFrEF, a total of 48 animals underwent the MI procedure. skmNox2^{KO} mice had a 30% higher post-operative survival than skmNox2$^{+/y}$ ($p = 0.026$) (Fig. 2B). Based on infarct size and right ventricle/body weight ratio inclusion criteria for severe HFrEF, we studied thirteen skmNox2$^{+/y}$ (one excluded) and nine skmNox2^{KO} (six excluded) HFrEF animals. Seventeen skmNox2$^{+/y}$ and thirteen skmNox2^{KO} animals comprised the sham surgery groups. The total number of animals used for diaphragm analysis was n = 52. Ventricular weights and fractional shortening displayed typical signs of HFrEF in infarcted animals compared to controls in both skmNox4 and 2 cohorts (Tables 1 and 2). There were no differences in cardiac function between HFrEF groups by experimental design.

3.2. Diaphragm contractile properties

In the skmNox4 cohort, HFrEF caused a 20% drop in maximal specific force, but this was fully prevented by skmNox4 KO (Fig. 3A, Table S1). There were significant surgery effects for HFrEF to decrease submaximal isometric contractions (twitch, Fig. 3B and 50 Hz, Table S1) with no protection by skmNox4 KO. There was a strain effect on 50 Hz contractions, with forces being higher in skmNox4KO (Table S1). Persistent reductions in submaximal force with HFrEF despite Nox4 KO suggested dysfunctional calcium handling which prompted assessment of the primary calcium release channel in skeletal muscle, the Ryanodine Receptor (RyR1). RyR1 protein abundance measured via immunoblotting decreased in HFrEF with no effect from skmNox4 KO (Fig. 3C).

In the skmNox2 cohort, we found that KO of Nox2 prevented about ½ of the decline in maximal specific force following myocardial infarction (Fig. 3A, Table S2). Multiple comparisons tests revealed significant differences between sham and MI groups in both the skmNox2$^{+/y}$ (15%; $p < 0.001$) and skmNox2^{KO} (7%; $p = 0.011$) groups. Comparing maximal specific force between HFrEF groups showed a significant difference for skmNox2$^{+/y}$ and skmNox2^{KO} ($p = 0.004$), which was not seen for Sham groups ($p = 0.731$). This indicates that skmNox2^{KO} partially protected the diaphragm from contractile dysfunction. Similar to the Nox4 cohort, there were significant surgery effects for HFrEF to decrease submaximal isometric forces (twitch, 30 Hz, and 50 Hz) (Fig. 3B and Table S2) regardless of strain.

3.3. Fiber type analysis and CSA

Animals in the Nox4 arm of experiments displayed no changes in cross sectional area or fiber type shifts with HFrEF or Nox4 KO (Figs. S2A and B). In the Nox2 arm of

experiments, there were no observable fiber type shifts (Fig. S2D), but the combination of skmNox2^{KO} and HFrEF prompted a decline in the percentage of type IIa fibers and an increase in Type IIx fibers compared to skmNox2^{KO} shams (Fig. S2E).

3.4. Mitochondrial respiration and content

Knockout of Nox4 increased mitochondrial J_{O_2} under conditions of submaximal ADP and Complex I + II supported-state 3 respiration (Fig. S3A). There were no observable strain or surgery effects for Respiratory control ratio (RCR) (skmNox4-sham: 6.4 ± 1.6; skmNox4-HFrEF: 6.1 ± 1.4; skmNox4^{KO}-sham: 6.6 ± 2.1; skmNox4^{KO}-HFrEF: 6.2 ± 1.5), citrate synthase abundance, or mitochondrial ETC complexes subunits (Fig. S4B).

In the skmNox2 cohort, there was a significant surgery effect for HFrEF to increase mitochondrial J_{O_2} under all conditions tested (Fig. S3B). RCR was not significantly different between groups (skmNox2-sham: 6.3 ± 2.0; skmNox2-HFrEF: 6.3 ± 1.4; skmNox2^{KO}-sham: 6.4 ± 1.9; skmNox2^{KO}-HFrEF: 6.1 ± 1.6). We also observed a significant surgery effect to decrease diaphragm citrate synthase content in HFrEF (Fig. S4D), while there were no apparent changes in abundance of subunits of mitochondrial electron transport chain complexes measured via immunoblotting (Fig. S4D).

3.5. Mitochondrial H_2O_2 emission and cellular redox tone

Mitochondrial H_2O_2 emission (baseline or succinate-induced) showed no significant differences in either the Nox4 or Nox2 cohort for the conditions tested (Fig. 4A and B). We assessed total and oxidized glutathione content in the Nox4 cohort upon finding full protection of maximal specific force. Oxidized glutathione increased with HFrEF ((Fig. 4D), while there were no statistically significance changes to GSH content (Fig. 4C).

4. Discussion

The principal findings from this study are that skeletal muscle-specific knockout of NAD(P)H Oxidase 4 (Nox4) provided full protection against the loss of diaphragm maximal specific force in HFrEF, whereas skeletal muscle-specific knockout of Nox2 incurred partial protection of maximal specific force. Neither Nox4 nor Nox2 skeletal muscle-specific knockout protected against the loss of submaximal force. Our study did not reveal increased mitochondrial ROS or diminished respiration as potential mechanism for diaphragm weakness and protection by Nox4 or Nox2. There was also no crosstalk between Nox and mitochondrial ROS examined from the perspective of either baseline or succinate-induced (complexes I and III) $J_{H_2O_2}$. Finally, knocking out Nox2 from skeletal myocytes increased survival post-myocardial infarction. These findings highlight a critical role for skeletal myocyte NAD(P)H Oxidases to influence maximal specific force (Nox4 and Nox2) and systemic pathophysiology (Nox2) in response following myocardial infarction.

4.1. Mouse model of HFrEF

Myocardial infarction (MI) is an established model of HFrEF with translational relevance [33,45]. The MI procedure has a survival rate of ~50%, with the majority of deaths occurring within 3–10 days [33,46, 47]. This expected survival rate agrees with guidelines

for experimental models of myocardial ischemia and infarction [34] and is in line with what we observed for the skmNox2$^{+/y}$, skmNox4$^{+/+}$ and skmNox4^{KO} MI groups. Interestingly, knockout of Nox2 in skeletal muscle cells increased survival post-MI to ~80% despite equivalent cardiac function and infarct sizes, as intended by experimental design. This finding suggests a role for skeletal myocyte Nox2 in influencing the systemic pathophysiology post-myocardial infarction, possibly through inflammatory signaling via skeletal myokines that modulate cardiac remodeling and the development of HFrEF (e.g., Ref. [48]). Increased survival was a serendipitous finding that is reported here for completeness and warrants future investigation. We were not prepared to examine survival post-MI and its related mechanisms. Our experimental design was focused on the chronic stage of HFrEF.

Because of the relationship between diaphragm weakness and disease severity [7], we proceeded with assays only in animals exhibiting signs of severe HFrEF based on RV weight-to-body weight ratio and infarct size. Per inclusion criteria, animals included in final analyses displayed typical signs of severe HFrEF (left and right ventricular hypertrophy, reduced fractional shortening, and a large infarcted area) that were not different following genetic recombination (KO vs. +/+). This is critical to compare direct effects on contractile function vs indirect effects due to disease modification.

4.2. *Diaphragm weakness – contractile function*

Diaphragm weakness is common in patients with severe HFrEF [1,2, 4]. The diaphragm is involved in inspiration and airway clearance maneuvers, and weakness in this muscle has been associated with the key HFrEF symptoms of dyspnea, fatigue, and exercise intolerance [1].

Diaphragm weakness in HFrEF can occur independent of muscle atrophy and is believed to be caused by excess production of ROS from unknown sources [1]. The decreases in diaphragm specific force observed in the HFrEF groups of this study (~20% for maximal specific force and twitch contractions) align with previous reports [7–9,11]. Skeletal muscle specific knockout of Nox2 provided partial protection to maximal specific force, while the knockout of Nox4 incurred full protection. The lack of full protection with skmNox2^{KO} suggests that Nox2 is partially required for the diaphragm weakness. It is possible that knockout of Nox2 results in compensatory responses from other sources of ROS. Indeed, knockout of the Nox2 subunit p47^{phox} leads to a compensatory increase in Nox4 [22]. The contribution of Nox4 to oxidant production may then be exacerbated with knockout of Nox2. In skmNox2KO animals, mRNA abundance of Nox4 increased with HFrEF, but did not reach significance ($p = 0.099$).

A previous study from our lab reported that whole-body knockout of the Nox2 complex organizing subunit p47^{phox} provides full protection of diaphragm maximal and submaximal force in the same mouse model of HFrEF employed here [9]. This contrasts with the findings of partial protection of maximal force and no protection of submaximal force with the skeletal muscle-specific knockout of the Nox2 subunit. There are several possibilities for this discrepancy: 1) whole-body knockout of p47^{phox} prevents the development of severe HFrEF and consequent diaphragm weakness. This appears unlikely because p47^{phox} KO

animals from the aforementioned study showed signs of more severe HFrEF compared to controls; 2) $p47^{phox}$ interacts with and influences Nox4 activity. While there are no reports of Nox4 associating with cytosolic subunits such as $p47^{phox}$, Nox4 does contain a $p47^{phox}$ binding motif [49]. $p47^{phox}$ KO could then prevent ROS production from both Nox2 and Nox4 leading to full protection of maximal and submaximal force in HFrEF; or 3) other cell types (i.e. vascular, neuronal, and immune) with high Nox2 activity contribute to diaphragm weakness, and these are still active with a skeletal muscle-specific intervention. Regardless, our study suggests that skeletal muscle-specific Nox4 plays a pivotal role in the development of diaphragm weakness, as seen in our findings of full protection of maximal specific force with $skmNox4^{KO}$.

The observation of consistently impaired submaximal force (1, 30, 50 Hz) in HFrEF, even with skmNox2 or skmNox4 KO, points to impaired Ca^{2+} handling or Ca^{2+} sensitivity of the myofilaments that have been reported in the diaphragm of rodents and humans with HFrEF [13,50–52]. Calcium release from the sarcoplasmic reticulum is a key determinant of peak twitch force. The RyR1 is the primary sarcoplasmic reticulum calcium release channel in skeletal muscle. Based on the loss of twitch force, we followed up with immunoblots of the RyR1 in the Nox4 cohort because this group experience full protection of maximal force. Our analysis showed that HFrEF decreased diaphragm RyR1 protein abundance and, consistent with data for twitch force, $skmNox4^{KO}$ did not prevent the decrease in RyR1 protein. Overall, our data suggests that decreased abundance (or dysfunction) of diaphragm RyR1 in HFrEF occurs independent of skeletal muscle-specific Nox2 and Nox4. In limb skeletal muscle, hyperphosphorylation of RyR1 impairs calcium handling and muscle contractile function in HFrEF [53]. Thus, mechanisms unrelated to ROS may be responsible for HFrEF-related impairments in calcium handling and loss of twitch force.

4.3. Diaphragm muscle cross-sectional area

Another potential contributor to diaphragm weakness in HFrEF is muscle atrophy [7,10,11,13], but this is not a consistent finding in rodents [8,52]. Diaphragm atrophy in HFrEF is associated with activation of proteolytic pathways, especially the ubiquitin-proteasome pathway [11,54]. We did not observe diaphragm atrophy in any of the HFrEF groups in our study. This discrepancy compared to other reports is possibly due to our mouse model of HFrEF, as multiple reports in larger mammals have observed diaphragm muscle atrophy in response to HFrEF [7,10,50]. Other explanations may be related to mouse sex (atrophy observed in female mice [11]) or strain (atrophy observed in CD-1 mice [55]). While atrophy has been reported in previous studies and occurs in humans, it does not contribute to the diaphragm weakness we observed herein and diaphragm fiber size in healthy mice was not modulated by skeletal muscle specific Nox2 or Nox4.

4.4. Reactive oxygen species and redox balance

Diaphragm weakness in HFrEF is linked to redox imbalance that promotes oxidation of myofibrillar and calcium handling proteins in skeletal muscle. In the skmNox4 cohort, we observed a significant increase in oxidized glutathione in diaphragm of HFrEF animals, accompanied by no change in reduced glutathione. This finding aligns with several previous reports of increased markers of oxidized shifts in redox balance in the diaphragm of HFrEF

patients and animal models [7,13,15,16], but the exact source of increased ROS or oxidized shift has not been resolved.

Nox4 mRNA abundance increased with HFrEF and this effect was prevented with skeletal muscle Nox4 KO. However, we did not observe increased mRNA abundance of Nox2 with HFrEF. Nox2 or Nox4 abundance may go through compensatory and temporal changes over the 16-week post-MI and in response to manipulation of redox-related enzymes. Indeed, a recent report demonstrated that whole-body knockout of $p47^{phox}$ (presumably preventing ROS from Nox2) was associated with a compensatory increase in abundance of Nox4 in skeletal muscle [22]. This certainly appears to be the case in our study as well, as knockout of Nox4 lowered mRNA abundance of Nox2 and p47phox, and knockout of Nox2 led to an increase in Nox4 (though not reaching the threshold for statistical significance). Importantly, our measurements of Nox2 and 4 mRNA were made with whole-muscle homogenates that contain other cell types, including vascular, neural, and immune cells that may influence our results and our study was not powered to resolve the Nox2-Nox4 mRNA crosstalk.

The mitochondrion is another skeletal muscle source of ROS, which may increase following mitochondrial dysfunction or signaling via cross-talk with other ROS sources [23]. Previous studies in rats showed increased mitochondrial H_2O_2 emission following myocardial infarction with methods that focused on the electron transport system in permeabilized diaphragm bundles [8,12,16]. There are reports of Nox4 localized to the mitochondria [19] and Nox4-induced complex I dysfunction [56]. Thus, we followed a similar approach as the aforementioned studies in HFrEF and examined succinate-induced (mainly complex I and III) mitochondrial ROS emission and found no significant differences due to HFrEF. This discrepancy suggests that either mouse diaphragm mitochondria undergo different adaptations to the rat, or the assay in mouse diaphragm fibers may not be sensitive enough to detect differences between sham and HFrEF. Importantly, there are additional sources of ROS production from the mitochondria beyond the succinate-induced effects explored here; mitochondria can produce ROS at any point along the electron transport system through electron leak, which is more likely to occur under conditions of elevated membrane potential, an elevated matrix NADH/NAD + ratio, and a reduced CoenzymeQ pool. These conditions largely result in greater superoxide production from complexes I and III, as well as matrix dehydrogenases [57]. It is worth noting that our assay includes superoxide dismutase to capture the emission of both superoxide and H_2O_2. We use the general term ROS because our goal was not to resolve specific species. In our setting, the baseline signal preceding addition of succinate could, in theory, lend insights into Nox2 or Nox4 derived ROS. There were no differences due to HFrEF or Nox2/Nox4 knockout on baseline $\dot{J}H_2O_2$. In our experience, the baseline signal from mouse diaphragm fibers is too low and has high variability that precludes conclusive resolution of the Nox2 or Nox4-derived ROS.

Finally, xanthine oxidase (XO) is an additional source of ROS within skeletal muscle that is worth mentioning in the context of muscle weakness in HFrEF. XO content increases in the early stage (72 h) of HFrEF in both diaphragm and limb muscle [31,58]. However, XO activity is not elevated long-term in limb muscle (days 7–28 post MI) and diaphragm XO content has not been explored in chronic HFrEF. One interpretation is that the mechanisms of muscle weakness are different in the early (up to 72 h) vs. late/chronic stage of HFrEF,

with XO playing predominant role in the early phase. Indeed, a recent study from our lab investigated diaphragm weakness 72 h post-MI and found no protection with whole-body KO of Nox4 [59], contrasting with our findings with skmNox4 KO in chronic HFrEF.

4.5. Limitations

There are several limitations to the current work. First, we did not measure Nox2 or 4 activity in skeletal muscle. Chemiluminescence assays have been used as a proxy for Nox activity, but their specificity has been questioned because experiments using a Nox1, Nox2, and Nox4 triple knockout showed no changes in chemiluminescence signal, which invalidates the assay [60]. A reliable Nox activity assay that is validated by appropriate positive and negative controls has not yet been developed. One promising option is a previously described fluorescent-linked p47phox reporter that is capable of indicating Nox2 activity and has been investigated in experimental settings deficient in p47phox and RAC1, both conditions predicted to lack a functional Nox2 complex [61, 62]. However, this would not be suitable for investigating Nox4 activity. Finally, our method to measure mitochondrial H_2O_2 emission and analyze crosstalk between Nox and mitochondrial-derived ROS is determined mainly by reverse electron transport and ROS emission from Complex I following the addition of succinate. There are several additional sites of ROS production within the mitochondria that cannot be excluded [57].

5. Conclusions

Our findings indicate that myocyte-specific Nox4 and Nox2 in the diaphragm are required for the loss of maximal but not submaximal specific force with HFrEF. Maximal inspiratory pressure, a measure of maximal diaphragm strength in humans, predicts adverse outcomes in patients with HFrEF. Thus, targeting skeletal muscle Nox4 or Nox2 could improve diaphragm strength and outcomes in patients with HFrEF but is unlikely to resolve all diaphragm contractile abnormalities caused by the disease. In our study, diaphragm weakness was not related to changes in muscle fiber type or atrophy, and succinate-induced mitochondrial H_2O_2 emission did not change in response to our genetic or surgical interventions. Finally, the knockout of Nox2 specifically from skeletal muscle increased survival post-myocardial infarction indicating a crucial role for skeletal muscle on the systemic pathophysiology following myocardial infarction.

Supplementary Material

Refer to Web version on PubMed Central for supplementary material.

Acknowledgments & Funding

The study was funded by NIH R01-HL130318. R. Kumar received a predoctoral fellowship from the American Heart Association (20PRE35200047). L. Ferreira was supported by an University of Florida Research Foundation Professorship and T. Ryan was funded by NIH R01-HL149704.

Abbreviations:

HFrEF	heart failure with reduced ejection fraction

References

[1]. Kelley RC, Ferreira LF, Diaphragm abnormalities in heart failure and aging: mechanisms and integration of cardiovascular and respiratory pathophysiology, Heart Fail. Rev 22 (2) (2017) 191–207. [PubMed: 27000754]

[2]. Mancini DM, LaManca JJ, Donchez LJ, Levine S, Henson DJ, Diminished respiratory muscle endurance persists after cardiac transplantation, Am. J. Cardiol 75 (5) (1995) 418–421. [PubMed: 7856545]

[3]. Hammond MD, Bauer KA, Sharp JT, Rocha RD, Respiratory muscle strength in congestive heart failure, Chest 98 (5) (1990) 1091–1094. [PubMed: 2225950]

[4]. Miyagi M, Kinugasa Y, Sota T, Yamada K, Ishisugi T, Hirai M, Yanagihara K, Haruki N, Matsubara K, Kato M, Yamamoto K, Diaphragm muscle dysfunction in patients with heart failure, J. Card. Fail 24 (4) (2018) 209–216. [PubMed: 29289723]

[5]. Ramalho SHR, Cipriano Junior G, Vieira PJC, Nakano EY, Winkelmann ER, Callegaro CC, Chiappa GR, Inspiratory muscle strength and six-minute walking distance in heart failure: prognostic utility in a 10 years follow up cohort study, PLoS One 14 (8) (2019), e0220638. [PubMed: 31369636]

[6]. Hamazaki N, Kamiya K, Yamamoto S, Nozaki K, Ichikawa T, Matsuzawa R, Tanaka S, Nakamura T, Yamashita M, Maekawa E, Meguro K, Noda C, Yamaoka-Tojo M, Matsunaga A, Ako J, Changes in respiratory muscle strength following cardiac rehabilitation for prognosis in patients with heart failure, J. Clin. Med. 9 (4) (2020).

[7]. Kelley RC, McDonagh B, Brumback B, Walter GA, Vohra R, Ferreira LF, Diaphragm weakness and proteomics (global and redox) modifications in heart failure with reduced ejection fraction in rats, J. Mol. Cell. Cardiol. (2020). S0022–2828(20)30026–2.

[8]. Laitano O, Ahn B, Patel N, Coblentz PD, Smuder AJ, Yoo JK, Christou DD, Adhihetty PJ, Ferreira LF, Pharmacological targeting of mitochondrial reactive oxygen species counteracts diaphragm weakness in chronic heart failure, J. Appl. Physiol. 120 (7) (2016) 733–742. [PubMed: 26846552]

[9]. Ahn B, Beharry AW, Frye GS, Judge AR, Ferreira LF, NAD(P)H oxidase subunit p47phox is elevated, and p47phox knockout prevents diaphragm contractile dysfunction in heart failure, Am. J. Physiol. Lung Cell Mol. Physiol. 309 (5) (2015) L497–L505. [PubMed: 26209274]

[10]. Howell S, Maarek JM, Fournier M, Sullivan K, Zhan WZ, Sieck GC, Congestive heart failure: differential adaptation of the diaphragm and latissimus dorsi, J. Appl. Physiol. 79 (2) (1995) 389–397. [PubMed: 7592193]

[11]. Adams V, Bowen TS, Werner S, Barthel P, Amberger C, Konzer A, Graumann J, Sehr P, Lewis J, Provaznik J, Benes V, Büttner P, Gasch A, Mangner N, Witt CC, Labeit D, Linke A, Labeit S, Small-molecule-mediated chemical knock-down of MuRF1/MuRF2 and attenuation of diaphragm dysfunction in chronic heart failure, J Cachexia Sarcopenia Muscle 10 (5) (2019) 1102–1115. [PubMed: 31140761]

[12]. Coblentz PD, Ahn B, Hayward LF, Yoo JK, Christou DD, Ferreira LF, Small hairpin RNA and pharmacological targeting of neutral sphingomyelinase prevents diaphragm weakness in rats with heart failure and reduced ejection fraction, Am. J. Physiol. Lung Cell Mol. Physiol. (2019).

[13]. Mangner N, Garbade J, Heyne E, van den Berg M, Winzer EB, Hommel J, Sandri M, Jozwiak-Nozdrzykowska J, Meyer A, Lehmann S, Schmitz C, Malfatti E, Schwarzer M, Ottenheijm C, Bowen TS, Linke A, Adams V, Molecular mechanisms of diaphragm myopathy in humans with severe heart failure, Circ. Res. (2021).

[14]. Tikunov B, Levine S, Mancini D, Chronic congestive heart failure elicits adaptations of endurance exercise in diaphragmatic muscle, Circulation 95 (4) (1997) 910–916. [PubMed: 9054750]

[15]. Ahn B, Coblentz PD, Beharry AW, Patel N, Judge AR, Moylan JS, Hoopes CW, Bonnell MR, Ferreira LF, Diaphragm abnormalities in patients with end-stage heart failure: NADPH oxidase upregulation and protein oxidation, Front. Physiol 7 (2016) 686. [PubMed: 28119629]

[16]. Supinski GS, Callahan LA, Diaphragmatic free radical generation increases in an animal model of heart failure, J. Appl. Physiol. 99 (3) (2005) 1078–1084. [PubMed: 16103520]

[17]. Henríquez-Olguín C, Boronat S, Cabello-Verrugio C, Jaimovich E, Hidalgo E, Jensen TE, The emerging roles of nicotinamide adenine dinucleotide phosphate oxidase 2 in skeletal muscle redox signaling and metabolism, Antioxidants Redox Signal 31 (18) (2019) 1371–1410.

[18]. Sakellariou GK, Vasilaki A, Palomero J, Kayani A, Zibrik L, McArdle A, Jackson MJ, Studies of mitochondrial and nonmitochondrial sources implicate nicotinamide adenine dinucleotide phosphate oxidase(s) in the increased skeletal muscle superoxide generation that occurs during contractile activity, Antioxidants Redox Signal 18 (6) (2013) 603–621.

[19]. Ferreira LF, Laitano O, Regulation of NADPH oxidases in skeletal muscle, Free Radic. Biol. Med. 98 (2016) 18–28. [PubMed: 27184955]

[20]. Winterbourn CC, Kettle AJ, Hampton MB, Reactive oxygen species and Neutrophil function, Annu. Rev. Biochem. 85 (2016) 765–792. [PubMed: 27050287]

[21]. Serrander L, Cartier L, Bedard K, Banfi B, Lardy B, Plastre O, Sienkiewicz A, Fórró L, Schlegel W, Krause K-H, NOX4 activity is determined by mRNA levels and reveals a unique pattern of ROS generation, Biochem. J. 406 (1) (2007) 105–114. [PubMed: 17501721]

[22]. Cully TR, Rodney GG, Nox4 - RyR1 - Nox2: regulators of micro-domain signaling in skeletal muscle, Redox Biol. 36 (2020), 101557. [PubMed: 32506037]

[23]. Dikalov S, Cross talk between mitochondria and NADPH oxidases, Free Radic. Biol. Med. 51 (7) (2011) 1289–1301. [PubMed: 21777669]

[24]. Sag CM, Schnelle M, Zhang J, Murdoch CE, Kossmann S, Protti A, Santos CXC, Sawyer G, Zhang X, Mongue-Din H, Richards DA, Brewer AC, Prysyazhna O, Maier LS, Wenzel P, Eaton PJ, Shah AM, Distinct regulatory effects of myeloid cell and endothelial cell NAPDH oxidase 2 on blood pressure, Circulation 135 (22) (2017) 2163–2177. [PubMed: 28298457]

[25]. McCarthy JJ, Srikuea R, Kirby TJ, Peterson CA, Esser KA, Inducible Cre transgenic mouse strain for skeletal muscle-specific gene targeting, Skeletal Muscle 2 (1) (2012) 8, 8. [PubMed: 22564549]

[26]. Kuroda J, Ago T, Matsushima S, Zhai P, Schneider MD, Sadoshima J, NADPH oxidase 4 (Nox4) is a major source of oxidative stress in the failing heart, Proc. Natl. Acad. Sci. USA 107 (35) (2010) 15565–15570. [PubMed: 20713697]

[27]. Saunders TL, Inducible transgenic mouse models, Methods Mol. Biol. 693 (2011) 103–115. [PubMed: 21080277]

[28]. Keefe AC, Lawson JA, Flygare SD, Fox ZD, Colasanto MP, Mathew SJ, Yandell M, Kardon G, Muscle stem cells contribute to myofibres in sedentary adult mice, Nat. Commun. 6 (2015) 7087, 7087. [PubMed: 25971691]

[29]. Pawlikowski B, Pulliam C, Betta ND, Kardon G, Olwin BB, Pervasive satellite cell contribution to uninjured adult muscle fibers, Skeletal Muscle 5 (2015) 42, 42. [PubMed: 26668715]

[30]. Virani SS, Alonso A, Aparicio HJ, Benjamin EJ, Bittencourt MS, Callaway CW, Carson AP, Chamberlain AM, Cheng S, Delling FN, Elkind MSV, Evenson KR, Ferguson JF, Gupta DK, Khan SS, Kissela BM, Knutson KL, Lee CD, Lewis TT, Liu J, Loop MS, Lutsey PL, Ma J, Mackey J, Martin SS, Matchar DB, Mussolino ME, Navaneethan SD, Perak AM, Roth GA, Samad Z, Satou GM, Schroeder EB, Shah SH, Shay CM, Stokes A, VanWagner LB, Wang NY, Tsao CW, Heart disease and stroke statistics-2021 update: a report from the American heart association, Circulation 143 (8) (2021) e254–e743. [PubMed: 33501848]

[31]. Scott Bowen T, Mangner N, Werner S, Glaser S, Kullnick Y, Schrepper A, Doenst T, Oberbach A, Linke A, Steil L, Schuler G, Adams V, Diaphragm muscle weakness in mice is early-onset post-myocardial infarction and associated with elevated protein oxidation, J. Appl. Physiol. 118 (1) (2015) 11–19. [PubMed: 25359720]

[32]. Finsen AV, Christensen G, Sjaastad I, Echocardiographic parameters discriminating myocardial infarction with pulmonary congestion from myocardial infarction without congestion in the mouse, J. Appl. Physiol. 98 (2) (2005) 680–689. [PubMed: 15475595]

[33]. Bayat H, Swaney JS, Ander AN, Dalton N, Kennedy BP, Hammond HK, Roth DM, Progressive heart failure after myocardial infarction in mice, Basic Res. Cardiol 97 (3) (2002) 206–213. [PubMed: 12061390]

[34]. Lindsey ML, Bolli R, Canty JM, Du XJ, Frangogiannis NG, Frantz S, Gourdie RG, Holmes JW, Jones SP, Kloner R, Lefer DJ, Liao R, Murphy E, Ping P, Przyklenk K, Recchia FA, Schwartz

Longacre L, Ripplinger CM, Van Eyk JE, Heusch G, Guidelines for experimental models of myocardial ischemia and infarction, Am. J. Physiol. Heart Circ. Physiol. (2018).

[35]. Kumar RA, Kelley RC, Hahn D, Ferreira LF, Dietary nitrate supplementation increases diaphragm peak power in old mice, J. Physiol. 598 (19) (2020) 4357–4369. [PubMed: 33460123]

[36]. Barclay CJ, Modelling diffusive O2 supply to isolated preparations of mammalian skeletal and cardiac muscle, J. Muscle Res. Cell Motil. 26 (4) (2005) 225–235. [PubMed: 16322911]

[37]. Close RI, Dynamic properties of mammalian skeletal muscles, Physiol. Rev. 52 (1) (1972) 129–197. [PubMed: 4256989]

[38]. Hahn D, Kumar RA, Ryan TE, Ferreira LF, Mitochondrial respiration and H2O2 emission in saponin-permeabilized murine diaphragm fibers: optimization of fiber separation and comparison to limb muscle, Am. J. Physiol. Cell Physiol. (2019).

[39]. Wen Y, Murach KA, Vechetti IJ Jr., Fry CS, Vickery C, Peterson CA, McCarthy JJ, Campbell KS, MyoVision: software for automated high-content analysis of skeletal muscle immunohistochemistry, J. Appl. Physiol. 124 (1) (2018) 40–51. [PubMed: 28982947]

[40]. Ferreira LF, Gilliam LAA, Reid MB, l-2-Oxothiazolidine-4-carboxylate reverses glutathione oxidation and delays fatigue of skeletal muscle in vitro, J. Appl. Physiol. 107 (1) (2009) 211–216. [PubMed: 19407260]

[41]. Jones DP, Redox potential of GSH/GSSG couple: assay and biological significance, Methods Enzymol. 348 (2002) 93–112. [PubMed: 11885298]

[42]. Wei J, Carroll RJ, Harden KK, Wu G, Comparisons of treatment means when factors do not interact in two-factorial studies, Amino Acids 42 (5) (2012) 2031–2035. [PubMed: 21547361]

[43]. Amrhein V, Greenland S, McShane B, Scientists rise up against statistical significance, Nature 567 (7748) (2019) 305–307. [PubMed: 30894741]

[44]. Curran-Everett D, Evolution in statistics: P values, statistical significance, kayaks, and walking trees, Adv. Physiol. Educ 44 (2) (2020) 221–224. [PubMed: 32412384]

[45]. Patten RD, Hall-Porter MR, Small animal models of heart failure, Circulation: Heart Fail. 2 (2) (2009) 138–144.

[46]. Gao E, Lei YH, Shang X, Huang ZM, Zuo L, Boucher M, Fan Q, Chuprun JK, Ma XL, Koch WJ, A novel and efficient model of coronary artery ligation and myocardial infarction in the mouse, Circ. Res. 107 (12) (2010) 1445–1453. [PubMed: 20966393]

[47]. Gao XM, Xu Q, Kiriazis H, Dart AM, Du XJ, Mouse model of post-infarct ventricular rupture: time course, strain- and gender-dependency, tensile strength, and histopathology, Cardiovasc. Res. 65 (2) (2005) 469–477. [PubMed: 15639486]

[48]. Henríquez-Olguín C, Altamirano F, Valladares D, López JR, Allen PD, Jaimovich E, Altered ROS production, NF-κB activation and interleukin-6 gene expression induced by electrical stimulation in dystrophic mdx skeletal muscle cells, Biochim. Biophys. Acta 1852 (7) (2015) 1410–1419. [PubMed: 25857619]

[49]. von Löhneysen K, Noack D, Wood MR, Friedman JS, Knaus UG, Structural insights into Nox4 and Nox2: motifs involved in function and cellular localization, Mol. Cell Biol. 30 (4) (2010) 961–975. [PubMed: 19995913]

[50]. Dominguez JF, Howell S, Compartmental analysis of steady-state diaphragm Ca2 + kinetics in chronic congestive heart failure, Cell Calcium 33 (3) (2003) 163–174. [PubMed: 12600803]

[51]. Hwee DT, Kennedy AR, Hartman JJ, Ryans J, Durham N, Malik FI, Jasper JR, The small-molecule fast skeletal troponin activator, CK-2127107, improves exercise tolerance in a rat model of heart failure, J. Pharmacol. Exp. Therapeut 353 (1) (2015) 159–168.

[52]. van Hees HWH, van der Heijden HFM, Ottenheijm CAC, Heunks LMA, Pigmans CJC, Verheugt FWA, Brouwer RMHJ, Dekhuijzen PNR, Diaphragm single-fiber weakness and loss of myosin in congestive heart failure rats, Am. J. Physiol. Heart Circ. Physiol. 293 (1) (2007) H819–H828. [PubMed: 17449557]

[53]. Wehrens XHT, Lehnart SE, Reiken S, van der Nagel R, Morales R, Sun J, Cheng Z, Deng S-X, de Windt LJ, Landry DW, Marks AR, Enhancing calstabin binding to ryanodine receptors improves cardiac and skeletal muscle function in heart failure, in: Proceedings of the National Academy of Sciences of the United States of America, vol. 102, 2005, pp. 9607–9612, 27. [PubMed: 15972811]

[54]. van Hees HWH, Li Y-P, Ottenheijm CAC, Jin B, Pigmans CJC, Linkels M, Dekhuijzen PNR, Heunks LMA, Proteasome inhibition improves diaphragm function in congestive heart failure rats, Am. J. Physiol. Lung Cell Mol. Physiol. 294 (6) (2008) L1260–L1268. [PubMed: 18424622]

[55]. Gillis TE, Klaiman JM, Foster A, Platt MJ, Huber JS, Corso MY, Simpson JA, Dissecting the role of the myofilament in diaphragm dysfunction during the development of heart failure in mice, Am. J. Physiol. Heart Circ. Physiol. 310 (5) (2016) H572–H586. [PubMed: 26702144]

[56]. Kozieł R, Pircher H, Kratochwil M, Lener B, Hermann M, Norbert A Dencher, P. Jansen-Dürr, Mitochondrial respiratory chain complex I is inactivated by NADPH oxidase Nox4, Biochem. J. 452 (2) (2013) 231–239. [PubMed: 23514110]

[57]. Murphy Michael P., How mitochondria produce reactive oxygen species, Biochem. J. 417 (1) (2009) 1–13. [PubMed: 19061483]

[58]. Nambu H, Takada S, Maekawa S, Matsumoto J, Kakutani N, Furihata T, Shirakawa R, Katayama T, Nakajima T, Yamanashi K, Obata Y, Nakano I, Tsuda M, Saito A, Fukushima A, Yokota T, Nio-Kobayashi J, Yasui H, Higashikawa K, Kuge Y, Anzai T, Sabe H, Kinugawa S, Inhibition of xanthine oxidase in the acute phase of myocardial infarction prevents skeletal muscle abnormalities and exercise intolerance, Cardiovasc. Res. 117 (3) (2021) 805–819. [PubMed: 32402072]

[59]. Hahn D, Kumar RA, Muscato DR, Ryan TE, Schröder K, Ferreira LF, Nox4 knockout does not prevent diaphragm atrophy, contractile dysfunction, or mitochondrial maladaptation in the early phase post-myocardial infarction in mice, Cell. Physiol. Biochem. 55 (4) (2021) 489–504. [PubMed: 34416105]

[60]. Rezende F, Löwe O, Helfinger V, Prior KK, Walter M, Zukunft S, Fleming I, Weissmann N, Brandes RP, Schröder K, Unchanged NADPH oxidase activity in Nox1-Nox2-Nox4 triple knockout mice: what do NADPH-stimulated chemiluminescence assays really detect? Antioxidants Redox Signal. 24 (7) (2016) 392–399.

[61]. Pal R, Basu Thakur P, Li S, Minard C, Rodney GG, Real-time imaging of NADPH oxidase activity in living cells using a novel fluorescent protein reporter, PLoS One 8 (5) (2013), e63989. [PubMed: 23704967]

[62]. Henríquez-Olguin C, Knudsen JR, Raun SH, Li Z, Dalbram E, Treebak JT, Sylow L, Holmdahl R, Richter EA, Jaimovich E, Jensen TE, Cytosolic ROS production by NADPH oxidase 2 regulates muscle glucose uptake during exercise, Nat. Commun. 10 (1) (2019) 4623. [PubMed: 31604916]

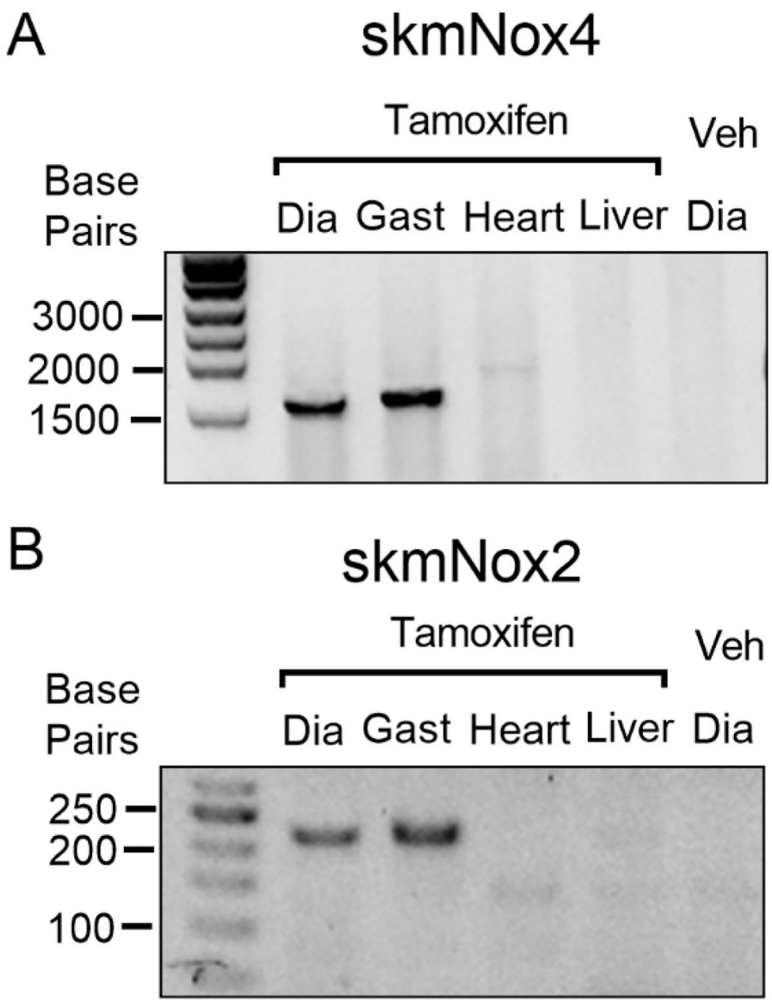

Fig. 1. Confirmation of Cre-induced genetic recombination.

(A, B) Representative gel images confirming genetic recombination in the diaphragm (Dia) and gastrocnemius (Gast) muscles of experimental animals receiving tamoxifen injections. Amplification of ~1600 base pair (bp) product in skmNox4 animals (A) and 225 bp product in skmNox2 animals (B). No recombination observed in the heart or liver of tamoxifen injected animals, or in the diaphragm from animals receiving control/vehicle injections.

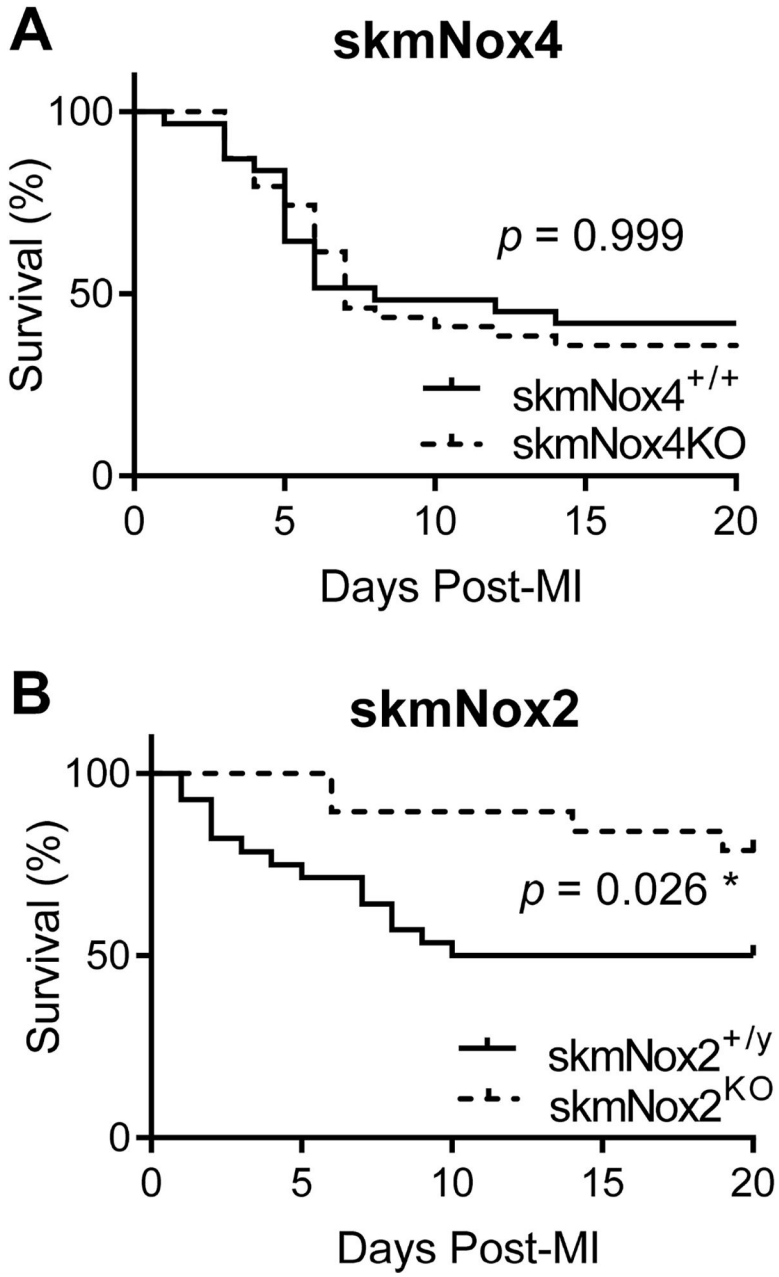

Fig. 2. Kaplan Meyer survival curves post-myocardial infarction.

Knockout of skeletal muscle Nox2 (B) but not Nox4 (A) improves survival post-myocardial infarction (MI). *P* values are from Gehan-Breslow-Wilcoxon test. **p* < 0.05.

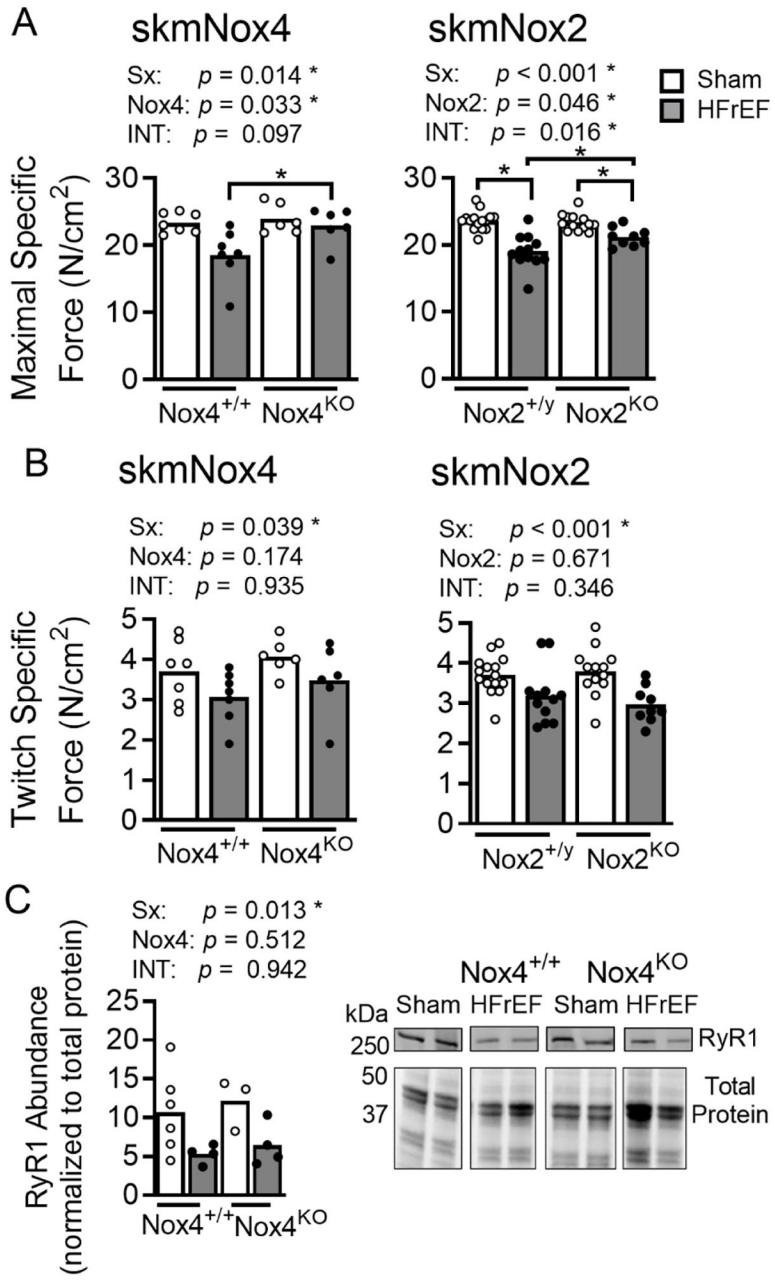

Fig. 3. Diaphragm isometric contractile properties and RyR abundance.

Maximal specific force (A) and twitch specific force (B) for skmNox4 and skmNox2 groups. (D) Diaphragm RyR abundance normalized to total protein (per lane). Images are representative membrane and total protein gel. Statistical analysis by two-way ANOVA with *p* values shown for effects of surgery (sham vs. HFrEF; Sx), Nox4 or Nox2, and the interaction of these two effects (Int). Bonferroni's post-hoc tests performed where appropriate. *$p < 0.05$.

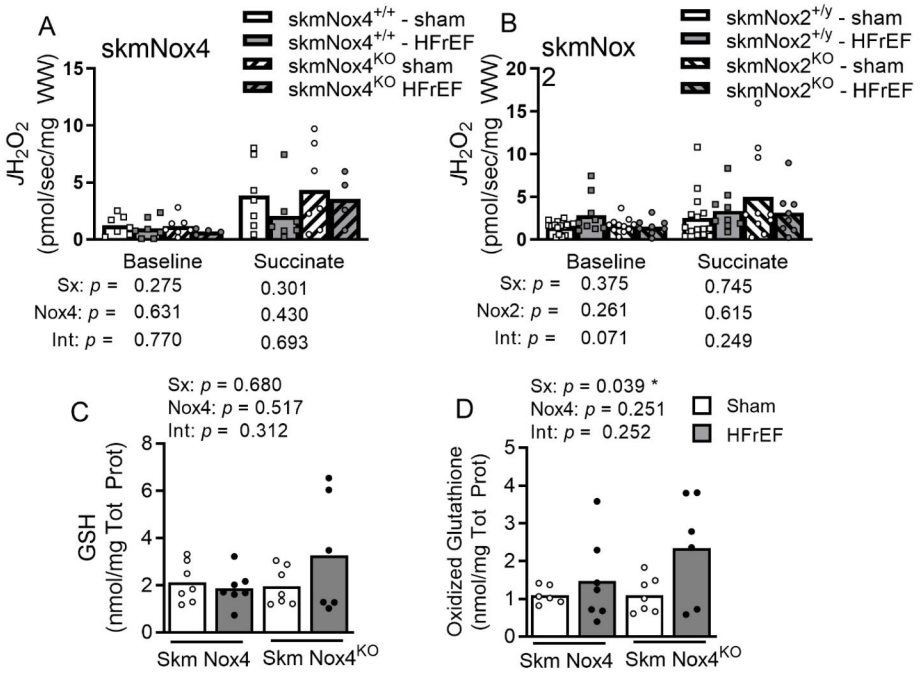

Fig. 4. Mitochondrial H_2O_2 emission and cellular redox tone.

Rate of hydrogen peroxide emission (JH_2O_2) measured in saponin-permeabilized diaphragm bundles for (A) skmNox4 and (B) skmNox2 groups. Diaphragm GSH (A) and Oxidized GSH (B) measured in the Nox4 cohort. Oxidized GSH calculated as the sum of CysGSH and 2 x GSSG. Statistical analysis by two-way ANOVA with *p* values shown for effects of surgery (sham vs. HFrEF; Sx), Nox4 or Nox2, and the interaction of these two effects (Int). $*p < 0.05$.

Table 1

skmNox4 - Animal characteristics.

	$SkmNox4^{+/+}$		$SkmNox4^{KO}$		*p* values		
	Sham (n = 7)	**HFrEF (n = 7)**	**Sham (n = 7)**	**HfrEF (n = 6)**	**Surgery**	**Nox4**	**Interaction**
Terminal body weight (g)	31.46 ± 2.7	30.9 ± 1.7	29.9 ± 3.1	30.5 ± 2.1	0.995	0.315	0.581
Fractional Shortening (%)	30.0 ± 4.6	13.5 ± 2.6	25.4 ± 5.5	15.5 ± 4.3	<0.001 *	0.473	0.067
LVIDD (cm)	0.45 ± 0.04	0.75 ± 0.10	0.48 ± 0.05	0.67 ± 0.13	<0.001 *	0.423	0.085
LVIDS (cm)	0.32 ± 0.04	0.65 ± 0.08	0.36 ± 0.05	0.57 ± 0.14	<0.001 *	0.587	0.072
Heart Rate (BPM)	424 ± 27	465 ± 66	443 ± 44	426 ± 67	0.567	0.637	0.176
Infarct size (%)	-	39 ± 5.7	-	42 ± 8.9	0.529		
RV weight (mg)	28 ± 2.8	48 ± 11.0	27 ± 2.8	44 ± 8.7	<0.001 *	0.331	0.555
LV weight (mg)	105 ± 8.7	188 ± 35.6	108 ± 12.6	202 ± 71.4	<0.001 *	0.665	0.953
RV weight/body weight	0.88 ± 0.04	1.57 ± 0.38	0.89 ± 0.11	1.44 ± 0.26	<0.001 *	0.611	0.506
LV weight/body weight	3.33 ± 0.15	6.10 ± 1.21	3.63 ± 0.43	6.7 ± 2.7	<0.001 *	0.414	0.871

Data are presented as mean ± SD. Statistical analysis by Two-way ANOVA with Bonferroni's post-hoc test when appropriate. Infarct size compared using Student's *t*-test. HFrEF, heart failure with reduced ejection fraction; LVID, left ventricular internal diameter during diastole (D) or systole (S); RV, right ventricle; LV, left ventricle.

* $p < 0.05$.

Table 2

skmNox2 - Animal characteristics.

	SkmNox2$^{+/y}$		**SkmNox2^{KO}**		***p* values**		
	Sham (n = 7)	**HFrEF (n = 7)**	**Sham (n = 7)**	**HfrEF (n = 6)**	**Surgery**	**Nox4**	**Interaction**
Terminal body weight (g)	34.7 ± 6.1	31.8 ± 2.9	37.2 ± 6.8	35.2 ± 6.1	0.074	0.149	0.713
Fractional Shortening (%)	26.7 ± 3.7	14.7 ± 8.2	29.3 ± 3.9	15.2 ± 5.3	<0.001 *	0.365	0.576
LVIDD (cm)	0.47 ± 0.09	0.62 ± 0.09	0.43 ± 0.03	0.71 ± 0.07	<0.001 *	0.245	0.008 *
LVIDS (cm)	0.35 ± 0.07	0.53 ± 0.12	0.31 ± 0.03	0.61 ± 0.08	<0.001 *	0.554	0.037 *
Heart Rate (BPM)	444 ± 69	459 ± 37	457 ± 54	470 ± 31	0.388	0.468	0.948
Infarct size (%)	-	38 ± 5.7	-	36 ± 6.1	0.514		
RV weight (mg)	28 ± 5.4	47 ± 11.8	26 ± 3.6	50 ± 9.9	<0.001 *	0.884	0.189
LV weight (mg)	116 ± 26.1	151 ± 18.5	108 ± 8.2	180 ± 39.0	<0.001 *	0.242	0.027 *
RV weight/body weight	0.82 ± 0.11	1.48 ± 0.42	0.71 ± 0.10	1.46 ± 0.38	<0.001 *	0.210	0.283
LV weight/body weight	3.36 ± 0.58	4.80 ± 0.70	2.97 ± 0.40	5.14 ± 0.90	<0.001 *	0.535	0.035 *

Data are presented as mean ± SD. Statistical analysis by Two-way ANOVA with Bonferroni's post-hoc test when appropriate. Infarct size compared using Mann- Whitney Ranked Sum test. HFrEF, heart failure with reduced ejection fraction; LVID, left ventricular internal diameter during diastole (D) or systole (S); RV, right ventricle; LV, left ventricle.

* $p < 0.05$.